

Competing quantum phases of hard-core boson with tilted dipole-dipole interaction

Huan-Kuang Wu¹ and Wei-Lin Tu²

¹*Department of Physics, Condensed Matter Theory Center and Joint Quantum Institute, University of Maryland, College Park, MD 20742, USA*

²*Institute for Solid State Physics, University of Tokyo, Kashiwa, Chiba 277-8581, Japan*
(Dated: December 22, 2024)

Different quantum phases of hard-core boson induced by dipole-dipole interaction with varying angles of polarization are discussed in this work. We consider the most influential two leading terms with anisotropy due to the tilted polarization of the on-site boson in the square lattice. For assuring the concreteness of our choice, we have applied both cluster mean-field theory (CMFT) and infinite projected entangled-pair state (iPEPS), and compared the results of our model with previous ones where longer-range interaction was included. Next, we focus on the case where the azimuthal angle is fixed to $\phi = \pi/4$. Through the mean-field analysis in a fashion that imposes quantum spin operators into classical ones, we aim to search for the underlying phases, especially the supersolid. Our results indicate a competing scenario between phases that break different translational symmetries. With the help of CMFT and variational iPEPS, the phase boundaries predicted by the mean-field treatment are determined more precisely. Our discoveries elucidate the possible underlying supersolid phases which might be seen in the real cold-atom experiments under dipolar interaction. Moreover, our results indicate that an effective triangular optical lattice can also be realized by fine tuning the dipolar angles.

I. INTRODUCTION

The ultracold atomic gases [1–4], thanks to the advance of cooling techniques, have become one of the promising platforms in studying various physical scenarios where quantum effect is emphasized. At such low temperature, exotic quantum phases could be formed due to the reduction of thermal fluctuation, and supersolid (SS), the state with coexisting superfluidity and solidity, is one of them [5, 6]. Recently, experimental groups have successfully captured the features that belong to SS from Bose-Einstein condensates, made of erbium and dysprosium gases, with large dipole moments [7–12]. Their discoveries have made huge impact to the physical society.

From the theoretical side, these ultracold atomic gases can be viewed as bosonic systems with soft- or hard-core characteristics, depending on the strength of the on-site repulsion. Under the hard-core limit, previous studies have shown that for a Hubbard-like Hamiltonian in square lattice, one will need more than nearest-neighbor (nn) interaction to stabilize the SS phases [13–16]. Similar effect can be seen by including the next-nearest-neighbor (nnn) hopping term [17, 18] and peculiar SS phases appear under the frustration. The effect of combining nnn hopping and interaction was discussed in Ref. 19 and our recent work has revealed that various superfluid (SF) and SS phases can be generated out of such extended Bose-Hubbard (EBH) Hamiltonian [20].

However, in the experiments mentioned above, the interaction between atoms is mediated by the dipole moment possessed by each boson [21]. These dipole moments, as demonstrated in Fig. 1, align along the direction of external electric/magnetic field and cast a long-range interaction of the following form:

$$V_{ij} = \frac{V}{r_{ij}^3} (1 - 3\cos^2\alpha_{ij}), \quad (1)$$

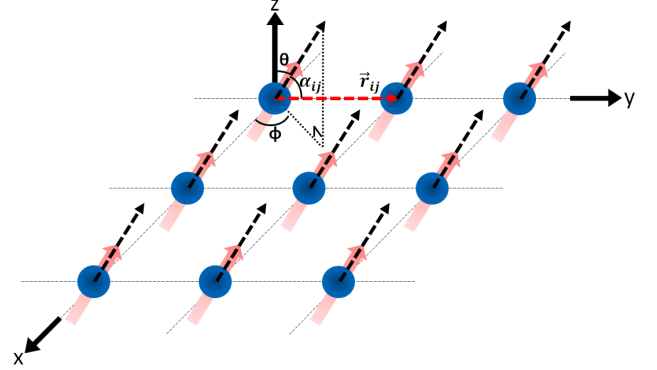


FIG. 1: Schematic demonstration of dipolar interaction in a two dimensional square optical lattice. Blue dots denote the atomic sites and pink arrows represent the polarization. Notice that in this work we consider the hard-core limit so that on each site there will be at most one boson. Polarization vector (black dashed vector) is determined by polar (θ) and azimuthal (ϕ) angles. α_{ij} determines the anisotropic dipolar interaction in Eq. 1 and can be obtained by measuring the angle between polarization and the vector of relative positions (red dashed vector) between two sites.

where V is the dipole-dipole interaction strength and $r_{ij} = |\vec{r}_i - \vec{r}_j|$, is the relative distance between site i and j . As demonstrated in Fig. 1, α_{ij} represents the angle between the vector of polarization and \vec{r}_{ij} , the relative-position vector from site i to site j . Due to the external field, all polarizations point to the same direction with identical polar (θ) and azimuthal (ϕ) angles. As can be seen from Eq. 1, if the polarization is along $\hat{e} = (0, 0, 1)$, then $\alpha_{ij} = \pi/2$ between every i and j so that the repul-

sive interaction becomes isotropic and decreases in inverse cubic form with r_{ij} throughout the optical lattice. Nonetheless, if we tilt the polarization to a non-zero polar angle, the interaction becomes anisotropic.

The effect of dipole-dipole interaction has been discussed previously for both isotropic [22–24] and anisotropic [25–28] cases in the hard-core limit for square lattice. For the scenarios with anisotropic interaction, however, studies were mainly focused on the polarization within the x-z(y-z) plane under different polar angles. In Ref. 28, the authors have mentioned the possible competition between two solid phases with intermediate azimuthal angle, which arouses our interest. In fact, according to Eq. 1, we can see that as α_{ij} changes from 90° to 0° , the dipolar interaction strength varies from V/r_{ij}^3 to $-2V/r_{ij}^3$, and is equal to zero at the transition angle $\cos^{-1}(1/\sqrt{3}) \approx 54.7^\circ$. If we choose ϕ to be $\pi/4$ and $35.3^\circ < \theta < \sin^{-1}(\sqrt{2}\cos(54.7^\circ)) \approx 54.8^\circ$, we can assure that the nn interaction is isotropically repulsive but the nnn interaction is attractive along the [1,1] direction while repulsive in the perpendicular direction. Under such circumstances, a diagonal stripe with 3×3 unit cell [22, 29] might be favored. Such effect of anisotropic nnn terms leading to the translational-symmetry breaking into a larger unit cell has been demonstrated before [30, 31]. Nevertheless, they analyzed the effect of nnn hopping terms, instead of the interactive terms. Moreover, although the dipole-dipole interaction is relatively long-range, due to the fact that its interaction strength decreases with distance in the inverse-cubic form, dominant short-range interactions are more influential in determining the resulting phases [32]. Therefore, we will focus on the effect of short-range interactions with realistic dipolar form, as indicated in Eq. 1.

This paper is organized in the following structure. In section II we will present our results. We first demonstrate our Hamiltonian and explain our numerical approaches in II.A. We then discuss the $\phi = 0$ case and present our results in II.B. Starting from II.C, we reveal our main results focusing on $\phi = \pi/4$. We will begin with a mean-field analysis to identify possible underlying phases, and a second-order perturbative approach to resolve the boundaries where solid order starts to melt down. We then perform the cluster mean-field theory to re-construct the phase diagrams. In order to attain the thermodynamic limit, we apply the variational iPEPS, which is more precise than the simple update. Our conclusion is included in section III.

II. RESULTS

A. Dipolar Bose-Hubbard Hamiltonian

Our Hamiltonian is chosen in the square lattice with the following form:

$$H = -t \sum_{\langle i,j \rangle} (b_i^\dagger b_j + H.C.) + \sum_{\langle i,j \rangle} V_1 n_i n_j + \sum_{\langle\langle i,j \rangle\rangle} V_2 n_i n_j - \mu \sum_i n_i, \quad (2)$$

with

$$V_1 = V(1 - 3\cos^2\alpha_{ij}) \\ V_2 = \frac{V(1 - 3\cos^2\alpha_{ij})}{2\sqrt{2}}, \quad (3)$$

where b_i^\dagger and b_i stand for the creation and annihilation operators of the hard-core boson, with the number operator to be $n_i = b_i^\dagger b_i$. $\langle i, j \rangle$ and $\langle\langle i, j \rangle\rangle$ denote the summation for the nn and nnn pairs, respectively. According to Eq. 1, our inter-site interactions, V_1 and V_2 , possess the forms indicated by Eq. 3. We neglect the further long-range tail of the dipolar interaction in this research.

We adopt two numerical methods for solving our model and the first one is the cluster mean-field theory (CMFT) [18, 24, 29, 33–40]. The central spirit is quite similar despite the varying details or namings among different references. We first divide our Hamiltonian into two parts. The first part, H_C , is within the chosen cluster, and the second part, $H_{\partial C}$, contains the terms connecting the bulk to the environment on the boundary of the cluster. H_C possesses the exact form of the original Hamiltonian (Eq. 2) and the mean-field decoupling only takes place in $H_{\partial C}$:

$$H_{\partial C} = -t \sum'_{\langle i,j \rangle} (b_i^\dagger \langle b_j \rangle + H.C.) + \sum'_{\langle i,j \rangle} V_1 n_i \langle n_j \rangle + \sum'_{\langle\langle i,j \rangle\rangle} V_2 n_i \langle n_j \rangle, \quad (4)$$

where the prime indicates that this summation is between site i on the boundary of the cluster and site j connected to i outside the cluster. Our effective Hamiltonian is then written as $H_{\text{eff}} = H_C + H_{\partial C}$. Next, we diagonalize the effective Hamiltonian and obtain the wave function for calculating the mean-field parameters, $\langle b_j \rangle$ and $\langle n_j \rangle$. After several iterations, the mean-field parameters converge and our calculation reaches its self-consistent solution. Note that the diagonalization only takes place within the chosen cluster.

The merit of CMFT is that, unlike the regular single-site mean-field calculation, CMFT can well cover the short-range correlation since the solution within the cluster is exact. By gradually enlarging the cluster size, we can extrapolate the results to the thermodynamic limit and a more precise phase boundary can be obtained

[18, 29, 35, 37]. In this work, for solving the exact Hamiltonian within the cluster, we have applied the exact diagonalization (ED).

In addition to CMFT, we have also employed another numerical ansatz for comparison, the infinite projected entangled-pair state (iPEPS) [41]. iPEPS has proven itself to be an effective ansatz for 2D quantum systems in a large scope [42]. For this ansatz, we use rank-5 tensors to demonstrate the wave function on each site within the repeating unit cell. Each tensor is composed of four auxiliary legs with dimension D and one physical index with dimension $d = 2$ here, reflecting the filled and empty states separately. Another merit of iPEPS is that we can achieve the properties in the thermodynamic limit. To attain the limit, we construct the environment tensors by applying the corner-transfer-matrix algorithm [43–45]. In our previous work [20], we have demonstrated that for extended Bose-Hubbard (EBH) model, simple-update iPEPS [46] is adequate for showing the correct structure of phase diagram. Therefore, we will try to apply the same approach here. However, later in section II.C.4, we will notice that for some regions where competing phases possess very close energies, it is hard for the simple-update iPEPS to distinguish them apart. There, we will apply another style of iPEPS, which is based on estimating the gradient of the variational energies to the tensor elements [47, 48].

B. $\phi=0$

First of all, we revisit the previously discussed case, where the polarization lies within the x-z(y-z) plane while tilting the polar angle. Here, we would like to investigate the influence by removing the long-range tail. For such polarization, the symmetry of nn interacting terms in x- and y-directions will break, while leaving the nnn interactions to be isotropic in our Hamiltonian:

$$\begin{aligned} V_x &= V \\ V_y &= V(1 - 3\sin^2\theta) \\ V_{nnn} &= \frac{V}{2\sqrt{2}}(1 - \frac{3}{2}\sin^2\theta). \end{aligned} \quad (5)$$

In Eq. 5, the polarization lies in the y-z plane. We then try to reconstruct the phase diagram shown in the Figure 2 of Ref. 28, which focused on the half-filled doping. In fact, their phase diagram already implies the dominant influence from nn and nnn interactions, because the checkerboard (CB) and stripe solids break the translational symmetry within the 2×2 unit cell, which is also the unit cell for V_{nn} and V_{nnn} interaction. Therefore, we expect that our phase diagram will be similar to theirs. Accordingly, we construct the phase diagram of half-filled phases using fixed- D simple-update iPEPS ($D=4$) and CMFT with 4×4 clusters. Our order pa-

rameter for charge order is defined as

$$\tilde{n}(\mathbf{k}) = \frac{1}{N_C} \sum_{i \in C} \langle n_i \rangle e^{i\mathbf{k} \cdot \mathbf{r}_i}, \quad (6)$$

and for the condensate density,

$$\rho_0 = \frac{1}{N_C} \sum_{i \in C} |\langle b_i \rangle|^2, \quad (7)$$

where C means the unit cell or cluster. r_i is the coordinate of location for each site. The zero-momentum condensate density, ρ_0 , indicates the superfluidity if a sharp peak exists. $\tilde{n}(\mathbf{k})$ reflects the structural order of bosons in the lattice. $\tilde{n}(\pi, \pi)$ represents the CB-like modulation and $\tilde{n}(\pi, 0)$ ($\tilde{n}(0, \pi)$) stands for stripe-like order. Our states can be classified by calculating these two orders. If there is no structural order then the state corresponds to SF; on the other hand, we have a CB/stripe solid state once structural order exists and $\rho_0 = 0$. These two orders, $\tilde{n}(\mathbf{k})$ for $\mathbf{k} \neq 0$ and ρ_0 , can coexist at the same time and a SS phase appears under such scenario.

Our result is shown in Fig. 2(a). The phase diagram for short-range dipolar interaction qualitatively agrees with the QMC result in Ref. 28. The black solid lines are phase boundaries obtained from CMFT. At small V/t , the system is in SF phase, characterized by a non vanishing condensate density ρ_0 . As V/t is increased, the system goes through a first order phase transition and either enters a CB solid or a stripe solid phase, depending on the anisotropy of the nn interaction determined by θ . Since the interaction is weaker for nnn bonds, CB is more favored for smaller θ . As θ increases, the anisotropy in nn interactions is enhanced. According to Eq. 5, when θ exceeds $\theta_c = \sin^{-1} \sqrt{2/(9 + 3\sqrt{2})}$, V_y becomes smaller than $2V_{nnn}$ and the stripe solid state oriented in the y direction becomes more favorable in the classical limit. θ_c is thus the critical polar angle in the limit $V/t \rightarrow \infty$, marked as the red triangle in Fig. 2(a). The phase transition between CB and stripe solid is first-order because of the breaking of different symmetries. Along this phase boundary, as V/t decreases, the kinetic energy becomes more important. From the perturbation points of view, the energy gain from hopping is $-t^2/2V_x - t^2/(4V_x - 2V_y)$ for CB solid and $-t^2/2V_x$ for stripe solid. This causes CB states to be more favorable, making the line lean to the right slightly at the triple point. Moreover, the phase boundaries by iPEPS (brown dashed lines in Fig. 2(a)) agree with those from CMFT, indicating that the underlying physics can be well represented by finite-size calculation. Most importantly, our calculations capture the correct phases revealed by QMC upon a full long-range dipolar model [28].

We next demonstrate the transitions across three phase boundaries along the cuts indicated by the black dotted lines in Fig. 2(a). Fig. 2(b) shows the condensate density and CB structural order parameters along the vertical cut $\theta = 0.2$. For smaller V/t , there is finite ρ_0 and no

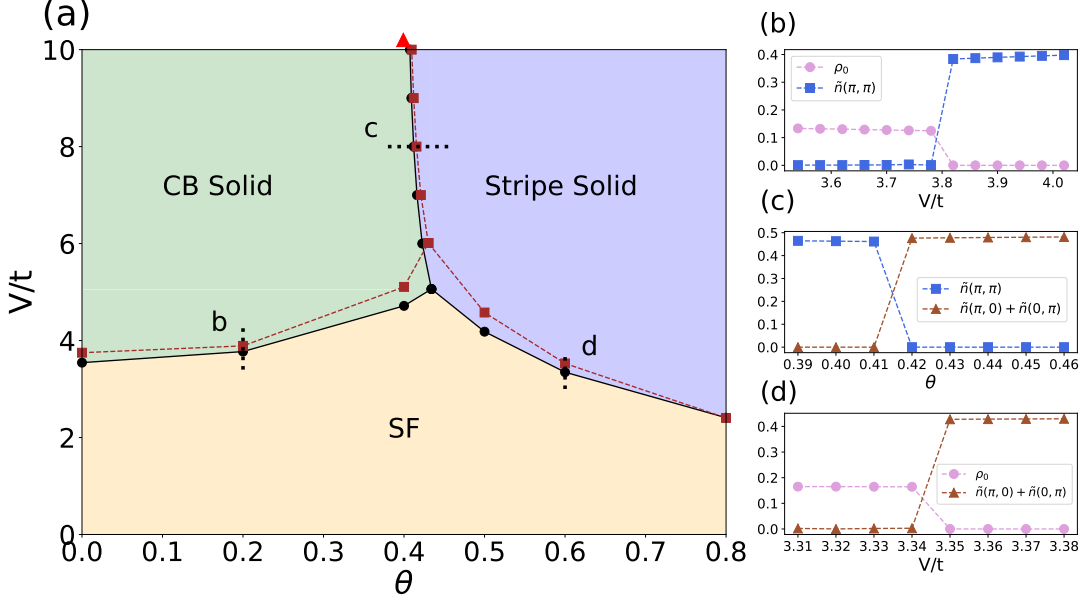


FIG. 2: (a) Phase diagram for half-filled phases for $\phi = 0$ obtained from CMFT (black solid line) and iPEPS (brown dashed line). The red triangle on top of the diagram indicates the critical polar angle, θ_c , between CB solid and stripe solid in the $V/t \rightarrow \infty$ limit. Order parameters by CMFT across three phase boundaries indicated by black dotted lines are plotted for (b) $\theta = 0.2$, (c) $V/t = 8$, and (d) $\theta = 0.6$.

CB structural factor, which represents a SF phase. At around $V/t \sim 3.8$, ρ_0 disappears with the simultaneous onset of $\tilde{n}(\pi, \pi)$, suggesting a first order transition to CB solid phase. Fig. 2(c) shows the CB and stripe structural factor along the horizontal cut at $V/t = 8$, where the two solid phases compete. Again, the order parameters indicate first-order features with an abrupt change from $\tilde{n}(\pi, \pi) \neq 0$ (CB solid) to $\tilde{n}(0, \pi) + \tilde{n}(\pi, 0) \neq 0$ (stripe solid) at around $\theta = 0.415$. At last, Fig. 2(d) is the vertical cut along $\theta = 0.6$. Similar to 2(b), the system starts from the SF phase with non-zero ρ_0 and vanishing $\tilde{n}(\pi, \pi)$, but it transits to stripe solid as $\tilde{n}(0, \pi) + \tilde{n}(\pi, 0)$ becomes finite at stronger interaction. The facts that all of our phase boundaries are first-order and no SS phase appears are in agreement with Ref. 28.

The above results show that our short-range dipolar Hamiltonian is able to reflect the same solid phases and behavior of the full dipolar model if the repeating unit cell is 2×2 , despite some quantitative differences. This accords with our expectation. The difference is that with the current Hamiltonian, we are not able to deal with the small plateaus, named after the Devil's staircase, in the $\mu - t$ phase diagram [22, 26]. These plateaus break higher symmetries under the long-range interaction, which is excluded here. However, in this work we strive to investigate the dominant phases and their properties. Therefore, it is reasonable to remove the longer-range tail in the current scope. After we present our main results in the next section, we will make a conjecture upon how our results would become under the true dipolar model, in the conclusion.

We conclude the discussion of short-range dipolar interaction with dipoles lying in the x-z(y-z) plane. Next, we will investigate its effect when azimuthal angle is set equal to $\pi/4$, where a more fruitful phase diagram would appear.

C. $\phi = \pi/4$

In contrast to the previous case, where polarization lies in the x-z(y-z) plane, by choosing $\phi = \pi/4$ we will have isotropic nn interacting terms, while nnn terms become anisotropic:

$$\begin{aligned}
 H = & -t \sum_{\langle i,j \rangle} (b_i^\dagger b_j + H.C.) + V_{nn} \sum_{\langle i,j \rangle} n_i n_j \\
 & + V_{[1,1]} \sum_{\langle\langle i,j \rangle\rangle_{[1,1]}} n_i n_j + V_{[1,-1]} \sum_{\langle\langle i,j \rangle\rangle_{[1,-1]}} n_i n_j \quad (8) \\
 & - \mu \sum_i n_i,
 \end{aligned}$$

where

$$\begin{aligned}
 V_{nn} &= V(1 - \frac{3}{2}\sin^2\theta) \\
 V_{[1,1]} &= \frac{V(1 - 3\sin^2\theta)}{2\sqrt{2}} \\
 V_{[1,-1]} &= \frac{V}{2\sqrt{2}}.
 \end{aligned} \quad (9)$$

$[1,1]/[1,-1]$ means the interaction along the $(1,1)/(1,-1)$ direction. Since we have set $\phi = \pi/4$ here, the interactive

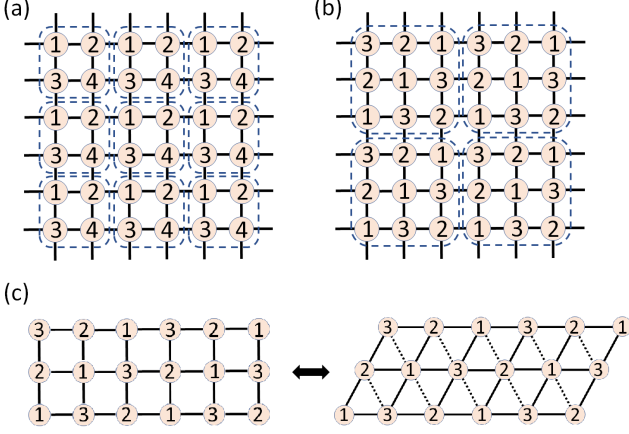


FIG. 3: Schematic demonstration of sublattice structures for (a) 2×2 and (b) 3×3 unit cell (dashed boxes) that we adopt for the mean-field analysis. For 2×2 unit cell we divide lattice sites into four different kinds, which guarantee to include all possible underlying structures. As for the 3×3 unit cell, we have three kinds of sublattices. (c) The equivalence of an eighteen-site square lattice to the effective triangular lattice with the same number of sites. Dotted lines indicate the virtual bonds where hopping is not allowed for bosons.

terms are expressed with one variable, the polar angle θ (Eq. 9). We will examine the effect of altering θ in this model. Note that according to Eq. 9, $V_{[1,-1]}$ is independent of θ while $V_{[1,1]}$ will alter with θ and change from repulsive to attractive interaction. We will then focus on the region of intermediate θ .

1. Mean-field analysis

To properly discuss possible underlying phases, it would be better to start from a mean-field analysis. The hard-core EBH model is known for its connection with spin-1/2 XXZ model under the mapping of $b_i^\dagger \rightarrow \hat{S}_i^+$, $b_i \rightarrow \hat{S}_i^-$, and $n_i \rightarrow \hat{S}_i^z + 1/2$ [49, 50]. Therefore, our Hamiltonian can be rewritten in the following form:

$$\begin{aligned}
 H = & -2t \sum_{\langle i,j \rangle} (\hat{S}_i^x \hat{S}_j^x + \hat{S}_i^y \hat{S}_j^y) + V_{nn} \sum_{\langle i,j \rangle} \hat{S}_i^z \hat{S}_j^z \\
 & + V_{[1,1]} \sum_{\langle\langle i,j \rangle\rangle_{[1,1]}} \hat{S}_i^z \hat{S}_j^z + V_{[1,-1]} \sum_{\langle\langle i,j \rangle\rangle_{[1,-1]}} \hat{S}_i^z \hat{S}_j^z \quad (10) \\
 & - (\mu - 2V_{nn} - V_{[1,1]} - V_{[1,-1]}) \sum_i \hat{S}_i^z.
 \end{aligned}$$

Now the Hamiltonian is represented with the pseudospin operator $\hat{\mathbf{S}}_i = (\hat{S}_i^x, \hat{S}_i^y, \hat{S}_i^z)$, which satisfies the commutation relation:

$$[\hat{S}_i^\mu, \hat{S}_j^\nu] = i\epsilon_{\mu\nu\lambda} \hat{S}_i^\lambda \delta_{ij}. \quad (11)$$

In contrast to the ordinary spin-1/2 XXZ model, Eq. 10 contains anisotropic interactive terms. For such spin model, the last term in Eq. 10 can be viewed as an effective external magnetic field with $h = \mu - 2V_{nn} - V_{[1,1]} - V_{[1,-1]}$. Related physical observables of the hard-core boson can be evaluated with $\langle n_i \rangle = \langle \hat{S}_i^z \rangle + 1/2$ and $\langle b_i \rangle = \langle \hat{S}_i^- \rangle$. Therefore, after the mapping, we can adopt the treatment of a spin model and then interpret our results back to the hard-core bosonic side.

At zero temperature, we can apply a mean-field treatment to the spin model by replacing the pseudospins with classical spin vectors with magnitude S equal to 1/2 [29]:

$$\hat{\mathbf{S}}_i \rightarrow \mathbf{S}_i^{cl} = S(\cos\varphi_i \sin\vartheta_i, \sin\varphi_i \sin\vartheta_i, \cos\vartheta_i). \quad (12)$$

After such transformation, we can calculate the classical mean-field energy, E^{MF} , of Eq. 10. We then minimize E^{MF} in the (ϑ, φ) space to determine the mean-field ground states. By investigating the different orders of these states, we can construct the mean-field phase diagrams.

The mean-field energy can be expressed in terms of different kinds of on-site pseudospin directions, depending on how many sublattices we have included. Note that to properly reproduce desired states with distinct structural order, we need to select a correct sublattice structure. Due to the rotational symmetry of local spin in the x-y plane, we can take $\varphi_i = 0$ for all sites without loss of generality. We then include four kinds of sublattices for the demonstration of states which break the translational symmetry within 2×2 unit cell. Its mean-field energy is:

$$\begin{aligned}
 E_4^{\text{MF}}/N = & -\frac{1}{4}t(\sin\vartheta_1 \sin\vartheta_2 + \sin\vartheta_1 \sin\vartheta_3 \\
 & + \sin\vartheta_2 \sin\vartheta_4 + \sin\vartheta_3 \sin\vartheta_4) \\
 & + \frac{1}{8}V_{nn}(\cos\vartheta_1 \cos\vartheta_2 + \cos\vartheta_1 \cos\vartheta_3 \\
 & + \cos\vartheta_2 \cos\vartheta_4 + \cos\vartheta_3 \cos\vartheta_4) \quad (13) \\
 & + \frac{1}{8}V_{[1,1]}(\cos\vartheta_1 \cos\vartheta_4 + \cos\vartheta_2 \cos\vartheta_3) \\
 & + \frac{1}{8}V_{[1,-1]}(\cos\vartheta_1 \cos\vartheta_4 + \cos\vartheta_2 \cos\vartheta_3) \\
 & - \frac{1}{8}h(\cos\vartheta_1 + \cos\vartheta_2 + \cos\vartheta_3 + \cos\vartheta_4),
 \end{aligned}$$

where the lower index of ϑ is the labeling of site within the unit cell. Note that we have already included the condition that $S = 1/2$ into our energy. In Ref. 29, the authors have also considered the 2×2 unit cell for only two sublattices, to describe the CB or stripe solid. But if we adopt four sublattices, then all possible underlying structures, such as CB, stripe, or quarter ($\rho = 1/4$ or $3/4$) solids, can be taken care of. This choice of sublattices is demonstrated in Fig. 3(a).

Because the dipolar interaction is anisotropic here, although our Hamiltonian contains terms no more than the next nearest neighbor, the stable states can still break the

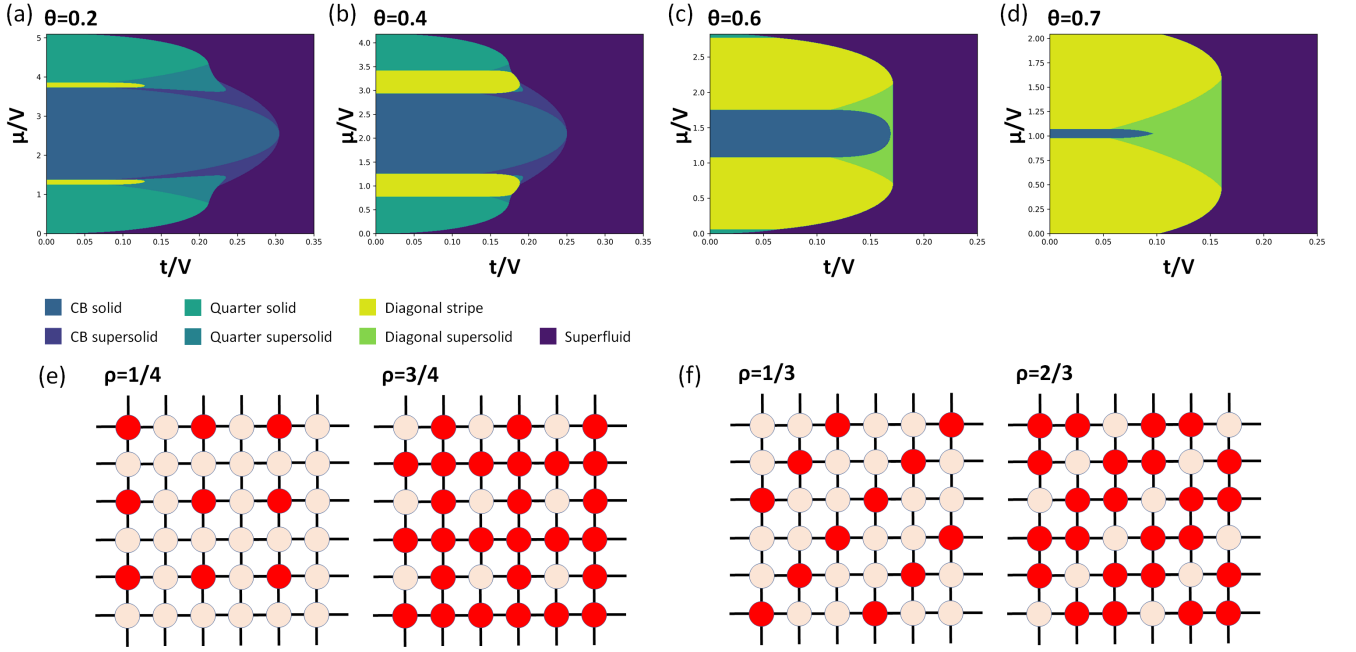


FIG. 4: Mean-field phase diagrams with polar angles (a) $\theta = 0.2$, (b) $\theta = 0.4$, (c) $\theta = 0.6$, and (d) $\theta = 0.7$. Figure legends are placed in the middle panel. Notice that in fact we have two quarter ($\rho = 1/4$ and $3/4$) and diagonal stripe ($\rho = 1/3$ and $2/3$) solids/SSs, but we label them with identical colors to demonstrate the particle-hole symmetry. (e) and (f) show the structures of these two quarter and diagonal stripe solids. Sites with darker color are the occupied sites and the others are for empty sites.

translational symmetries of larger unit cell. Ref. 30 has shown that such anisotropy can lead to the symmetry breaking within the 3×3 unit cell, which is in fact effectively equivalent to the triangular lattice [51]. For our model, we expect that such equivalence would appear as the effect of nnn interacting term in one direction ($V_{[1,1]}$) becomes more dominant than the other ($V_{[1,-1]}$), while it varies from repulsion to attraction along with the polar angle θ . To address such states, we write down our mean-field energy by including three sublattices, as shown in Fig. 3(b):

$$\begin{aligned}
 E_3^{\text{MF}}/N = & -\frac{1}{3}t(\sin\vartheta_1\sin\vartheta_2 + \sin\vartheta_1\sin\vartheta_3 + \sin\vartheta_2\sin\vartheta_3) \\
 & +\frac{1}{6}V_{nn}(\cos\vartheta_1\cos\vartheta_2 + \cos\vartheta_1\cos\vartheta_3 + \cos\vartheta_2\cos\vartheta_3) \\
 & +\frac{1}{12}V_{[1,1]}(\cos^2\vartheta_1 + \cos^2\vartheta_2 + \cos^2\vartheta_3) \\
 & +\frac{1}{12}V_{[1,-1]}(\cos\vartheta_1\cos\vartheta_2 + \cos\vartheta_1\cos\vartheta_3 + \cos\vartheta_2\cos\vartheta_3) \\
 & -\frac{1}{6}h(\cos\vartheta_1 + \cos\vartheta_2 + \cos\vartheta_3).
 \end{aligned} \tag{14}$$

Such three-sublattice structure is in fact equivalent to an effective triangular lattice, shown in Fig. 3(c). The diagonal bonds are virtual since our Hamiltonian does not include the nnn hopping. However, the nnn interactions,

$V_{[1,1]}$ and $V_{[1,-1]}$, can still be present in between diagonal bosons. Other kinds of symmetry breaking for larger unit cells will require the inclusion of longer-range interaction. Note that in this work we do not consider the possibility of incommensurately ordered phases. We will then use the mean-field energies in Eq. 13 and 14 to construct the phase diagrams under different polar angles. Since these two energies have different minimum values, we need to search for the ground-state energies for both cases and then compare the values to decide which one should be the true ground state.

From Fig. 4(a) to (d) we plot the mean-field phase diagrams for different polar angles. It is clear that diagonal stripe appears gradually once the polar angle is more tilted. At $\theta = 0.6$, quarter solid/SS is almost replaced by diagonal stripe solid. Moreover, in between the lobes of CB and diagonal solids, diagonal SS is formed, replacing the CB SS. Previously, we have mentioned that when the polar angle θ is tilted more than $35.3^\circ \approx 0.616$, $V_{[1,1]}$ becomes attractive and is more in favor for the formation of diagonal stripe solid. This can be seen as we further tilt the polar angle to 0.7, and diagonal stripe becomes the dominant phase while CB solid only occupies a very small area in the middle of phase diagram. Its area will keep shrinking until no phase that breaks 2×2 translational symmetry can be seen in the phase diagram. If we further tilt the polar angle, then after $\theta \approx 0.956$, even nn interaction becomes attractive. As a result, the phase

diagram becomes trivial for $\mu > 0$, where bosons tend to occupy all sites.

Notice that unlike the case when polarization is within the x-z(y-z) plane, we cannot find any traditional stripe phase all along the tilting. This can be demonstrated by comparing the mean-field energies of CB and stripe solids, setting $\cos\vartheta_1 = \cos\vartheta_4 = -\cos\vartheta_2 = -\cos\vartheta_3 = 1$ for CB and $\cos\vartheta_1 = \cos\vartheta_2 = -\cos\vartheta_3 = -\cos\vartheta_4 = 1$ for stripe:

$$E_4^{\text{MF(CB)}}/N = -\frac{1}{2}V_{nn} + \frac{1}{4}(V_{[1,1]} + V_{[1,-1]}), \quad (15)$$

and

$$E_4^{\text{MF(stripe)}}/N = -\frac{1}{4}(V_{[1,1]} + V_{[1,-1]}). \quad (16)$$

Since the condition for forming the stripe solid is that $E_4^{\text{MF(CB)}} > E_4^{\text{MF(stripe)}}$, therefore we obtain $V_{nn} < V_{[1,1]} + V_{[1,-1]}$. Then according to Eq. 9, the condition becomes $\theta \gtrsim 0.955$, where the states that break 2×2 translational symmetry are no longer prominent. As a result, no stripe solid/SS can be formed.

In fact, by analyzing the mean field energy, the phase boundaries and whether they are first- or second-order transitions can be determined analytically. This has been discussed for 2×2 unit cell in Ref. [29]. Here, we will provide a similar analysis on the complementary case for the 3×3 supercell. This will be done by examining the mean-field energy E_3^{MF} in Eq. 14. Since under the particle-hole transformation ($\vartheta_i \rightarrow \vartheta_i + \pi, i = 1, 2, 3$), all terms remain the same except for the Zeeman field $h \rightarrow -h$, we only have to consider the lower-half of the phase diagram where h is negative. In this case, the three states to be considered are SF ($\vartheta_1 = \vartheta_2 = \vartheta_3$), $1/3$ diagonal stripe ($\vartheta_1 = 0, \vartheta_2 = \vartheta_3 = \pi$) and the diagonal SS (all the others). Let us first look at the stability of the diagonal stripe and SF. This is determined by the signs of the eigenvalues of the Hessian matrix $\mathbf{H}_{i,j}(\vartheta_1, \vartheta_2, \vartheta_3) = \partial^2 E_3^{\text{MF}} / \partial \vartheta_i \partial \vartheta_j$. If a state is stable (at the local minimum), both eigenvalues will be positive; otherwise the state is unstable. Therefore, at the stability boundaries, we expect $\det(\mathbf{H})(\vartheta_1, \vartheta_2, \vartheta_3) = 0$, where one of the eigenvalues becomes zero.

For diagonal stripe phase, the corresponding pseudospin coordinate $(\vartheta_1, \vartheta_2, \vartheta_3)$ is at $(0, \pi, \pi)$, while for the SF, $(\vartheta_1, \vartheta_2, \vartheta_3) = (\psi, \psi, \psi)$, where $\psi = \cos^{-1}(h/4t + 2V_{nn} + V_{[1,1]} + V_{[1,-1]})$. This is the position that minimizes E_3^{MF} along $\vartheta_1 = \vartheta_2 = \vartheta_3$. Plugging in these two conditions separately, we found that the stability boundary for diagonal stripe satisfies:

$$8t^2 + (2t + V_{[1,1]} + h)(2V_{nn} - V_{[1,1]} + V_{[1,-1]} + h) = 0, \quad (17)$$

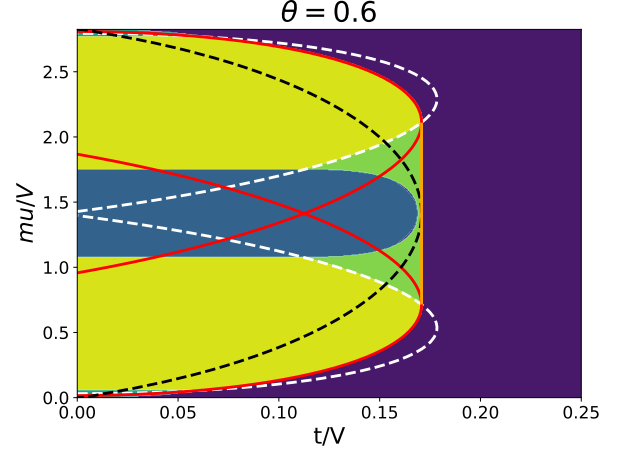


FIG. 5: Analytic phase boundaries for tilting angle $\theta = 0.6$. For comparison, we adopt the corresponding phase diagram in Fig. 4(c) as the background. Boundaries indicated by solid(dashed) curves are of first(second) order. The white dashed lines enclose regions where diagonal stripe solid is stable, while the local minima of SF persist outside the black dashed curve. Red(Orange) solid curves(line) represent the points of energy crossover between diagonal stripe solid(SS) and SF, where the enclosed area on the left-hand side always breaks translational symmetry.

and for the SF:

$$\begin{aligned} & h^4(4t + 2V_{nn} - 2V_{[1,1]} + V_{[1,-1]}) \\ & + 2h^2(4t + 2V_{nn} + V_{[1,1]} + V_{[1,-1]})^2 \\ & \times (2t - 2V_{nn} - V_{[1,-1]} + 2V_{[1,1]}) \\ & - (4t + 2V_{nn} + V_{[1,1]} + V_{[1,-1]})^4 \\ & \times (8t - 2V_{nn} + 2V_{[1,1]} - V_{[1,-1]}) = 0. \end{aligned} \quad (18)$$

In Fig. 5, we take the case of polar angle $\theta = 0.6$ as an example to demonstrate different analytical boundaries. Besides the first-order boundaries surrounding the checkerboard solid and quarter solid phase, all the other phase boundaries can be accounted for within our analysis. First, the two stability boundaries mentioned above are presented as dashed lines. The white dashed lines enclose two regions where diagonal stripe solid is stable; on the contrary, the region outside the enclosed area by black dashed line denotes the SF stability. Since these stability lines represent the spontaneous symmetry breaking in the parameter space, they are in fact second-order boundaries.

Since the diagonal stripe solid and SF states break different symmetries, the phase boundaries in between them must be of first order, and thus do not belong to continuous dashed boundaries. In this case, we would need to compare the energies of the two states to determine the boundaries. Their analytic form can be derived by sim-

ply setting $E_3^{MF}(0, \pi, \pi) = E_3^{MF}(\psi, \psi, \psi)$, which results in the formula:

$$12t - 2V_{nn} + 3V_{[1,1]} - V_{[1,-1]} + 2h + \frac{3h^2}{4t + 2V_{nn} + V_{[1,1]} + V_{[1,-1]}} = 0. \quad (19)$$

This corresponds to the red solid lines in Fig. 5. Note that since the conditions for diagonal stripe solid and SF states cannot be interchanged continuously in the phase space, these are indeed first-order boundaries, agreeing with the argument from the symmetry point of view. Combining the above deductions, we can conclude that the intersecting areas enclosed by the red solid curves and the white dashed curves represent the phase of diagonal stripe solid.

Finally, the boundary between diagonal SS and SF is less obvious due to the fact that the diagonal SS does not have a strong constraint for its degrees of freedom like the other two cases. However, we notice that the tips of two red solid curves and black dashed curve are all located at a vertical straight line, which is

$$t = \frac{2V_{nn} + V_{[1,-1]} - 2V_{[1,1]}}{8}. \quad (20)$$

Plugging this back into Eq. (14), the mean field energy becomes

$$\begin{aligned} E_3^{MF} &= \frac{2V_{nn} + V_{[1,-1]} - V_{[1,1]}}{24} [(\sin \vartheta_1 - \sin \vartheta_2)^2 \\ &\quad + (\sin \vartheta_2 - \sin \vartheta_3)^2 + (\sin \vartheta_3 - \sin \vartheta_1)^2] \\ &+ \frac{2V_{nn} + V_{[1,-1]}}{24} \left(\sum_i \cos \vartheta_i - \frac{2h}{2V_{nn} + V_{[1,-1]}} \right)^2 \\ &+ \frac{2V_{[1,1]} - 2V_{nn} - V_{[1,-1]}}{8} - \frac{h^2}{6(V_{[1,-1]} + 2V_{nn})}. \end{aligned} \quad (21)$$

According to the above form, there are two global minima in the phase space where the first two terms vanishes. One is a SF state at $\vartheta_1 = \vartheta_2 = \vartheta_3 = \cos^{-1}(2h/(6V_{nn} + 3V_{[1,-1]}))$ and the other is a diagonal SS on $\vartheta_1 = \pi - \vartheta_2 = \pi - \vartheta_3$ with $\vartheta_1 = \cos^{-1}(-2h/(2V_{nn} + V_{[1,-1]}))$. As a result, the straight line of Eq. (20), denoted by orange color in Fig. 5, indicates the first-order boundary between diagonal SS and SF. Note that the point of intersection between orange line and black dashed curve is a highly symmetrical point, where the breaking of translational symmetry can take place continuously. Similar first-order transition between diagonal SS and SF is also observed in Refs. 35 and 51 and it can not be directly inferred from the symmetry argument. At last, since the states within 3×3 unit cell compete with those in 2×2 unit cell, part of the phase boundaries is replaced by the one caused from the phase competition. Note that since these competing phases always break different symmetries, the phase boundaries are of first order.

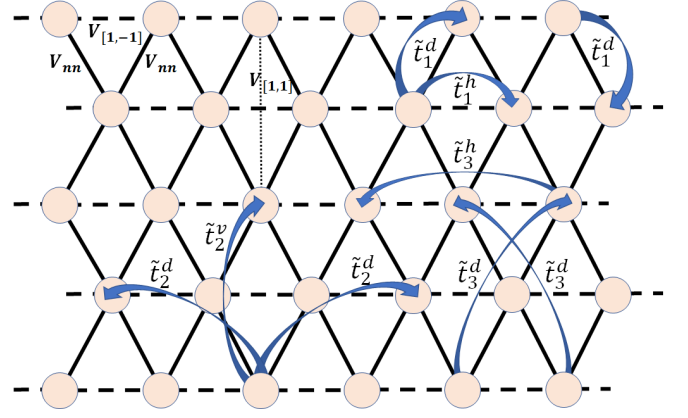


FIG. 6: Schematic demonstration of interaction and hopping terms after mapping to the effective triangular lattice. V_{nn} lies on the diagonal bonds and $V_{[1,-1]}/V_{[1,1]}$ lies on the virtual horizontal(dashed)/vertical(dotted) bonds. Hopping terms for the second-order perturbation theory are also plotted for nearest, next-nearest, and next-next-nearest neighbor, which are generated by two-step processes.

In sum, our mean-field analysis reveals that the physical scenario we discuss here can be interpreted as the competition between states belonging to square and effectively triangular lattices. This is largely different from the previous case when polarization is within the plane of principal axis.

2. Defect condensation

Our mean-field analysis has revealed the existence of solid and SS which are absent as the polarization stays along the principal axes. This also includes the diagonal SS state from the three-sublattice scenario. Therefore, it is worthy to investigate more of the effective triangular lattice along with the related phases, and the perturbation theory is helpful for showing the phase transition from solid to SS [51]. Because the SS is formed by doping the commensurate solid, called the "defect-condensation" [19], we can think of doping as adding defects into the background composed of a perfect solid. By studying the energy of defect we can determine the transition points where having defects within lattice is more stable, leading to the formation of SS. For that purpose, first we need to write down the effective model for the defects.

Since now we focus on the effective triangular lattice, original interaction terms on the square lattice is now mapped into the form shown in Fig. 6. For the nearest two sites interaction exists along the diagonal (V_{nn}) and horizontal ($V_{[1,1]}$) directions, while $V_{[1,-1]}$ corresponds to the interaction across the diamond. Due to the particle-hole symmetry for the hard-core boson we only analyze the scenario when bosons are doped as defects into the $1/3$ diagonal stripe. For such scenario, defects lie on a

honeycomb lattice where the centers of all hexagons are occupied with bosons [51]. The effective Hamiltonian for defects is then:

$$\begin{aligned}
H = & - \sum_{i,n,\alpha} \tilde{t}_n^\alpha (a_i^\dagger a_{i+1} + H.C.) + V_{nn} \sum_{\langle i,j \rangle} m_i m_j \\
& + V_{[1,1]} \sum_{\langle\langle i,j \rangle\rangle_{[1,1]}} m_i m_j + V_{[1,-1]} \sum_{\langle\langle i,j \rangle\rangle_{[1,-1]}} m_i m_j \\
& - \tilde{\mu} \sum_i m_i,
\end{aligned} \tag{22}$$

where $m_i = a_i^\dagger a_i$ is the number operator for defects. \tilde{t}_n^α has two sub-indices and $n \in [1, 2, 3]$, representing the nearest, next-nearest, and next-next-nearest hoppings, respectively. For $n = 1$ or 3 , $\alpha \in [h, d]$, meaning the hoppings along horizontal or diagonal direction. While as $n = 2$, $\alpha \in [v, d]$, reflecting the hoppings in vertical or diagonal direction. Details are shown in Fig. 6. We will then expand these hopping terms up to the second order of perturbation, generated from the two-step process of hoppings. Their forms are expressed in the following context. For $n = 1$:

$$\begin{aligned}
\tilde{t}_1^h &= \frac{t^2}{V_{[1,-1]} - V_{[1,1]}} \\
\tilde{t}_1^d &= t,
\end{aligned} \tag{23}$$

$n = 2$:

$$\begin{aligned}
\tilde{t}_2^v &= \frac{t^2}{V_{[1,-1]} - V_{[1,1]}} \\
\tilde{t}_2^d &= 0,
\end{aligned} \tag{24}$$

and $n = 3$:

$$\begin{aligned}
\tilde{t}_3^h &= 0 \\
\tilde{t}_3^d &= \frac{t^2}{V_{[1,-1]} - 2V_{[1,1]}}.
\end{aligned} \tag{25}$$

The two-step process will also alter the effective chemical potential, leading to $\tilde{\mu} = \mu - 2V_{nn} - V_{[1,-1]} + \mu^{(2)}$, where

$$\begin{aligned}
\mu^{(2)} = & \frac{t^2}{V_{nn} - V_{[1,1]}} + \frac{3t^2}{V_{[1,-1]} - V_{[1,1]}} \\
& + \frac{2t^2}{V_{nn} - 2V_{[1,1]}} + \frac{2t^2}{V_{[1,-1]} - 2V_{[1,1]}} \\
& + \frac{2t^2}{2V_{nn} + V_{[1,-1]} - 2V_{[1,1]}} \\
& - \frac{14t^2}{V_{nn} + V_{[1,-1]} - 2V_{[1,1]}}.
\end{aligned} \tag{26}$$

Knowing the forms of parameters in the effective Hamiltonian, now we can check the stability of solid by introducing a single defect. The ground state energy, E_G , is located at the Γ point and for $t > 0$:

$$E_G = -\tilde{t}_1^h - 2\tilde{t}_1^d - 2\tilde{t}_2^v - 2\tilde{t}_3^d - \tilde{\mu}. \tag{27}$$

This energy will change sign crossing the transition points. As a result, we obtain the phase boundary as a curve of $\mu - t$ between solid and SS:

$$\mu = 2V_{nn} + V_{[1,-1]} - \mu^{(2)} - \tilde{t}_1^h - 2\tilde{t}_1^d - 2\tilde{t}_2^v - 2\tilde{t}_3^d. \tag{28}$$

This phase boundary of perturbation theory is shown in Fig. 7 of the next section, along with our numerical outcomes for a clearer comparison.

3. CMFT phase diagrams

To better determine the phase boundaries, we have also performed the CMFT calculation to construct again the phase diagrams. We focus on the scenarios of $\theta = 0.7$ and $\theta = 0.8$, where the diagonal SS phase is more pronounced, as shown in Fig. 7(a) and 7(b). Results are obtained from considering the ground state of 3×3 and 4×4 clusters, which can host states that possess a 2×2 unit cell. For the first-order transitions, we determine the phase boundaries by extrapolating the energy on the two sides and then finding the intersection. On the other hand, the second-order phase boundary between diagonal solid and diagonal SS is defined as the onset of superfluidity, which can be obtained by extrapolating the condensate density on the SS side to zero. The analytic boundaries between solid and SS obtained from defect condensation (Eq. 28) are also shown for comparison.

At small μ , the system at $t = 0$ is in the diagonal stripe phase, characterized by a non-vanishing order $S_{diag} \equiv |\tilde{n}(2\pi/3, 2\pi/3) + \tilde{n}(2\pi/3, -2\pi/3)|$. As t increases, it goes through a first-order phase transition to SF. The first-order nature is characterized by a discontinuous drop in dE/dt , as can be seen in Fig. 7(c), where a horizontal cut along $\mu = 0$ for Fig. 7(b) is shown.

As μ becomes larger, a diagonal SS phase appears between the solid and SF phase, where both S_{diag} and ρ_0 are present. As an example, the cut along $\mu = 0.4$ is shown in Fig. 7(d). Focusing on the dE/dt curve, we observed a discontinuous drop at the transition point from SS to SF, indicating a first-order phase transition. This is consistent with the aforementioned mean-field result. The discontinuity reduces as μ increases and disappears at the symmetry point, $\mu = 2V_{nn} + V_{[1,1]} + V_{[1,-1]}$, where the transition becomes second-order. We do not observe such drop in dE/dt at the onset of superfluidity from diagonal stripe phase, which suggests that the transition from solid to SS is of second order. In Fig. 7(a) and (b), the phase boundaries between solid and SS, obtained by defect condensation, are plotted as blue dashed curves, showing good agreement with the CMFT counterparts. It suggests that the perturbation theory performs well in this transition. At $\theta = 0.7$, a CB solid phase appears as the chemical potential approaches the symmetry point. Since the CB solid breaks different translational symmetry, the phase boundary is also first-order. This again confirms the competing picture that we have revealed by the mean-field analysis.

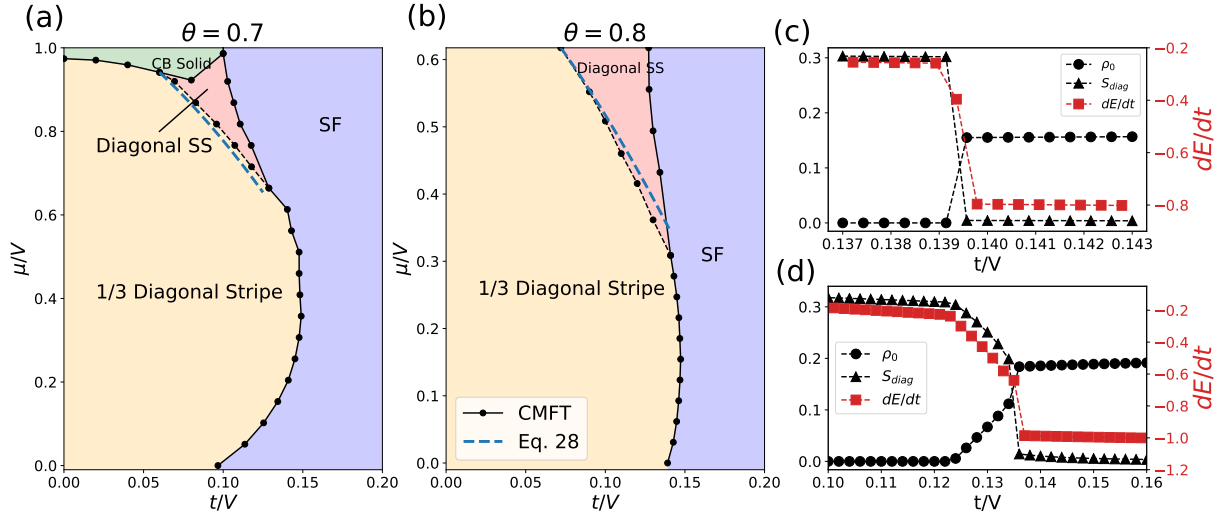


FIG. 7: (a), (b) : Phase diagrams for (a) $\theta = 0.7$ and (b) $\theta = 0.8$ obtained by CMFT. The blue-dashed lines are the analytic phase boundaries between diagonal stripe solid and diagonal SS from the analysis of defect condensation in Eq. 28. (c), (d) : Two horizontal cuts at $\theta = 0.8$ for (c) $\mu = 0$ and (d) $\mu = 0.4$. In (c), a clear first order phase transition between diagonal solid and SF can be seen from the dE/dt curve. In (d), the phase transition between diagonal solid and SS is of second order, while that between SS and SF is of first order.

Comparing Fig. 7(a) with its corresponding mean-field phase diagram in Fig. 4(d), different phase boundaries are quite consistent except for the one between SS and SF, where the mean-field theory overestimates the SS regions. This is due to the fact that mean-field approaches ignore the effect of quantum fluctuation, which is unfavorable for long-range orders. In our model, quantum fluctuation becomes the strongest when the effective external field h approaches zero. Therefore, the mean-field phase boundary is the least accurate in this regime.

4. Thermodynamic limit

An important issue we need to investigate is if the above phases obtained by mean-field-based methods can be stable after pushing to the thermodynamic limit. Of course, this can be done by gradually increasing the cluster size in the CMFT and performing the scaling technique, which will be shown in the Appendix. But here, we apply another strategy and use iPEPS for this purpose. However, we have noticed that the simple-update iPEPS is no longer enough for the reason that these phases possess competing energies very close to each other and it is hard to distinguish them without a more precise ansatz. Therefore, we turn to another kind of iPEPS, which is based on the variational way of optimization [47, 48]. For this kind of iPEPS, we firstly encode the full progress among obtaining the variational energy of the target Hamiltonian, starting from the wavefunctions in the form of tensors. We then apply the backward-propagated automatic differentiation (AD) to calculate the gradients of our target function, the variational en-

ergy, and then optimize the wavefunctions. In this way, we do not have to go through the traditional process of optimization where estimation after singular value decomposition (SVD) happens repeatedly.

Fig. 8 represents the results of our variational iPEPS with bond dimension $D = 4$. In Fig. 8(a), we go through a vertical cut at $t/V = 0.085$ in Fig. 7(b). In the middle we can see clearly a region where condensate density (ρ_0) coexists with solid order S_{diag} , indicating the existence of diagonal SS. We enlarge the region encircled by black dotted box and it is clear that at $\tilde{n}(0,0) \approx 0.5$ there is a two-fold degeneracy. This is because our two diagonal stripe solids are in analogy to the Ising spins under external magnetic field. When μ is larger than the symmetric point (effective field pointing upward), the state prefers the one with more bosons (spin aligning upward), and μ being smaller than the symmetric point (effective field pointing downward) is the other way around. Such effect can be more clearly seen in the inset of Fig. 8(b), where the cut along $t/V = 0.06$ is drawn. Due to the above-mentioned reason, the quantum state will resume half-filled only when the solid order is smeared out; that is to say, when entering the SF phase. As a result, SS can not be half-filled in the current scope since its solid order is not zero. This conclusion is the same as that in Ref. 28.

Fig. 8(b) shows another vertical cut along $t/V = 0.12$. An obvious first-order phase transition can be seen between diagonal solid and superfluid, indicated by a sudden jump of order parameters. To reveal the competition between phases of different sublattices, we plot the cut of $t/V = 0.085$ for $\theta = 0.7$. Along this cut, diagonal stripe solid melts into diagonal SS, right before the solid order

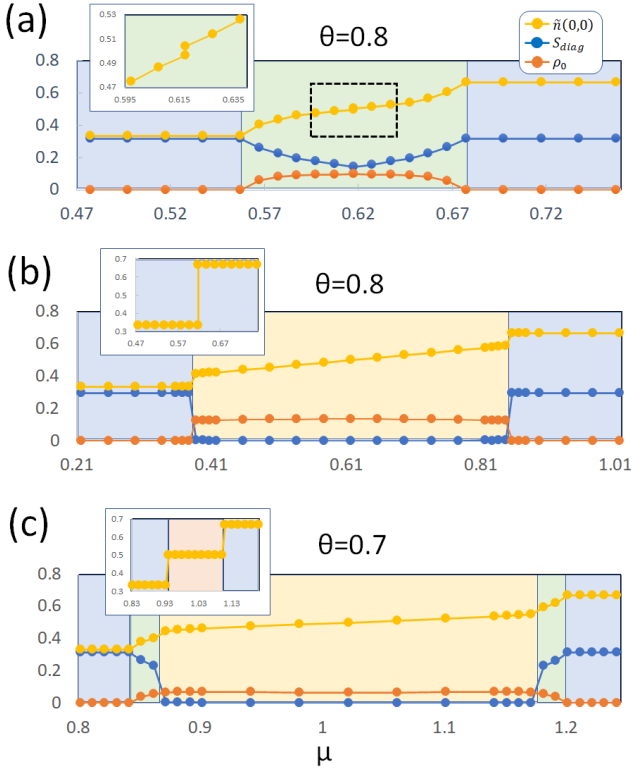


FIG. 8: iPEPS data for order parameters $\tilde{n}(0,0)$, S_{diag} , and ρ_0 . In (a), the cut is along $t/V = 0.085$ for $\theta = 0.8$. Green area marks the region for SS phase while solid phases are indicated with blue background. The inset magnifies the region enclosed by black dotted box in the middle. In (b), the cut is now along $t/V = 0.12$. For this cut, SS is replaced by SF denoted by yellow background. Its inset shows a cut along $t/V = 0.06$. For $\theta = 0.7$, a cut along $t/V = 0.085$ is present in (c). The inset demonstrates again a cut for $t/V = 0.06$, where competition between CB and diagonal stripe solids takes place.

is completely smeared out with a first-order transition into the superfluid. However, unlike the CMFT phase diagram, we do not see the phase competition here. We then plot another cut along $t/V = 0.06$ in the inset for showing the competition between different solid phases. It is clear that diagonal stripe solid transits into CB solid with a first-order phase transition. Here, we apply the variational iPEPS with different unit cells, in order to obtain both states. We then compare their energies to determine the ground state, as what we have done in the mean-field analysis.

We have noticed that some differences appear in comparison with the CMFT phase diagrams. For example, in Fig. 8(c) the SS phase goes through a first-order phase transition into the superfluid. However, in Fig. 7(a), SS would directly transit into checkerboard solid in the same cut. This indicates the overestimation of SS phase from CMFT, which is not surprising because mean-field

treatment has this tendency. Recall that we mentioned CMFT can capture the short-range correlation within the cluster, but for SF it contains the off-diagonal long-range order (ODLRO). Therefore, within a finite cluster such long-range effect is underestimated, while the solid order is properly described if the cluster is larger than its unit cell.

Among all, a more detailed investigation from iPEPS, such as enlarging the bond dimension, may be able to provide a more precise phase diagram much closer to the real experiments. We will, nevertheless, leave this part in future works since in this article we mainly focus on elucidating the competition between phases and their identifications.

III. CONCLUSION

In this work, we have considered the short-range dipolar model with tilting polar angles. For the polarization lying in the x-z(y-z) plane, we have re-constructed the similar phase diagram as shown in Ref. [28] with CMFT and simple-update iPEPS. By setting the dipole moment pointing along the direction with $\phi = \pi/4$ while varying the polar angle, we have discovered that the physical scenario is in fact the competition among phases belonging to different unit cells. Moreover, the diagonal stripe and its SS correspond to quantum states in an effective triangular lattice. Thus, our results reveal the possibility to generate a scenario for triangular optical lattice out of the original square lattice, with the fine tuning of dipolar angle.

Previously, we have mentioned that the difference between our model and the long-range dipolar model is that the so-called Devil's staircase is excluded in the short-range model. In addition to this, it is common for some SS phases to become destabilized for the short-range model due to the strong quantum fluctuation [29]. Nevertheless, our main phases in Section II.C are shown to be present in the thermodynamic limit. We therefore expect that our SS phases can exist for the full long-range dipolar model. Moreover, we have noticed that for isotropic dipolar interaction, the diagonal stripe solid can already be seen [22]. Therefore, under the long-range model, the diagonal stripe could become the prominent phase at smaller θ than our prediction.

Since we have known that for $\phi = 0$ the similar competition exists only within the 2×2 unit cell, with the appearance of stripe solid for $\theta \gtrsim 0.5$, we estimate that for some intermediate ϕ the competition between CB and diagonal solids would be replaced by the competition between stripe and diagonal solids, as varying the polar angle. But since we do not expect any new phase except the stripe solid and its SS with the current Hamiltonian (Eq. 8), we did not examine other ϕ values here. We believe a more interesting scenario would be gradually increasing the interactive range, where an interpolation to the long-range physics can be realized and yet avoid-

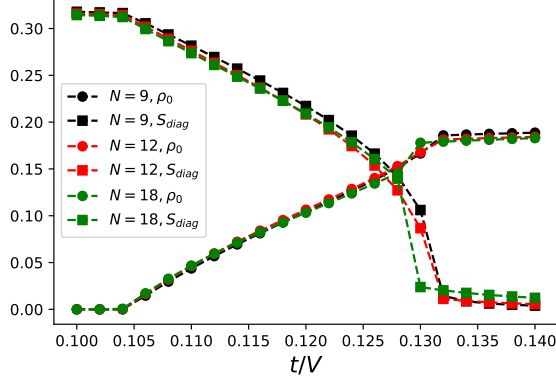


FIG. A.1: Order parameters for different cluster along line cut $\mu = 0.494$ at $\theta = 0.8$.

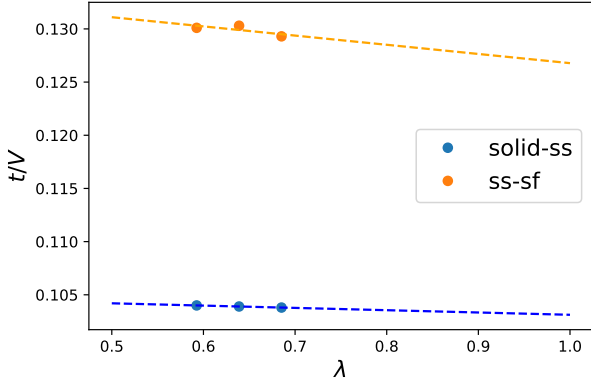


FIG. A.2: Scaling analysis for the phase boundaries in Fig. A.1. The scaling parameter λ is defined using the effective triangular lattice.

ing the hard-to-tract Devil's staircase [52]. Of course, a true long-range model is believed to reflect the most underlying physics. Therefore, a more detailed research considering also the long-range interaction with the help of QMC, is left for future consideration.

IV. ACKNOWLEDGEMENT

H.-K.W. is supported by JQI-NSF-PFC (supported by NSF grant PHY-1607611). W.-L.T. is supported by Post-

doctoral Research Abroad Program, Project No. 108-2917-I-564-007, from Ministry of Science and Technology (MOST) of Taiwan.

Appendix A: Scaling analysis of CMFT

In CMFT calculations, the effect of correlation with range beyond the cluster size is excluded. To infer the physics in the thermodynamic limit, a common method is to repeat the calculation on clusters of different sizes and perform extrapolation. We employ the scaling method introduced in Refs. 29 and 35, with the scaling parameter λ defined as $\lambda \equiv N_B/(N_C \times z/2)$, where N_B is the number of nn bonds, N_C is the number of sites, and z is the coordination number for the lattice. Since $\lambda \rightarrow 1$ in the thermodynamic limit, we can approach this limit by extrapolating λ to 1.

Here we examine the phase boundary for diagonal SS as $\lambda \rightarrow 1$. We choose the line cut along $\mu = 0.494$ at $\theta = 0.8$, where the diagonal SS phase can be found between $0.104 < t/V < 0.13$ in the 3×3 cluster, as shown in Fig. 7(b). Besides the 9-site cluster, we have conducted the calculation with 12- and 18-site clusters. The 12-site cluster is a 3×4 rectangular lattice and the 18-site cluster is a 45° -tilted square lattice defined by the side vectors $(3, 3)$ and $(3, -3)$. Results are shown in Fig. A.1, where the order parameters from these three clusters are consistent with each other, except when approaching the SS-SF transition point. We notice that SS phase becomes thinner as cluster size increases, which accords with the observation by iPEPS.

The finite-size scaling is performed for the phase boundaries. Since the phases appearing here are from the equivalent triangular lattice, we instead adopt the lattice structure in Fig. 3(c) to define the scaling parameter λ . The result is shown in Fig. A.2. According to the linear extrapolation, at $\lambda = 1$ the ss-sf(solid-ss) transition point is at $t/V \sim 0.1031(0.1268)$. These values are reasonably close to those from the 3×3 cluster, which are 0.1040 and 0.1301. Therefore, we can conclude that the 3×3 cluster already provides a good estimation for the CMFT.

-
- [1] I. Bloch, J. Dalibard, and W. Zwerger, "Many-body physics with ultracold gases," *Rev. Mod. Phys.* **80**, 885 (2008).
 - [2] I. Bloch, J. Dalibard, and S. Nascimbne, "Quantum simulations with ultracold quantum gases," *Nature Phys.* **8**,

267 (2012).

- [3] P. Windpassinger and K. Sengstock, "Engineering novel optical lattices," *Rep. Prog. Phys.* **76**, 086401 (2013).
- [4] M. Tomza, K. Jachymski, R. Gerritsma, A. Negretti, T. Calarco, Z. Idziaszek, and P. S. Julienne, "Cold hy-

- brid ion-atom systems,” *Rev. Mod. Phys.* **91**, 035001 (2019).
- [5] M. Penrose and L. Onsager, “Bose-Einstein Condensation and Liquid Helium,” *Phys. Rev.* **104**, 576 (1956).
 - [6] M. Boninsegni and N. V. Prokof’ev, “Colloquium: Supersolids: What and where are they?” *Rev. Mod. Phys.* **84**, 759 (2012).
 - [7] L. Tanzi, E. Lucioni, F. Fam, J. Catani, A. Fioretti, C. Gabbanini, R. N. Bisset, L. Santos, and G. Modugno, “Observation of a Dipolar Quantum Gas with Metastable Supersolid Properties,” *Phys. Rev. Lett.* **122**, 130405 (2019).
 - [8] F. Bttcher, J. N. Schmidt, M. Wenzel, J. Hertkorn, M. Guo, T. Langen, and T. Pfau, “Transient Supersolid Properties in an Array of Dipolar Quantum Droplets,” *Phys. Rev. X* **9**, 011051 (2019).
 - [9] L. Chomaz, D. Petter, P. Ilzhfer, G. Natale, A. Trautmann, C. Politi, G. Durastante, R. M. W. van Bijnen, A. Patscheider, M. Sohmen, M. J. Mark, and F. Ferlaino, “Long-Lived and Transient Supersolid Behaviors in Dipolar Quantum Gases,” *Phys. Rev. X* **9**, 021012 (2019).
 - [10] G. Natale, R. M. W. van Bijnen, A. Patscheider, D. Petter, M. J. Mark, L. Chomaz, and F. Ferlaino, “Excitation Spectrum of a Trapped Dipolar Supersolid and Its Experimental Evidence,” *Phys. Rev. Lett.* **123**, 050402 (2019).
 - [11] L. Tanzi, S. M. Roccuzzo, E. Lucioni, F. Fam, A. Fioretti, C. Gabbanini, G. Modugno, A. Recati, and S. Stringari, “Supersolid symmetry breaking from compressional oscillations in a dipolar quantum gas,” *Nature* **574**, 382 (2019).
 - [12] M. Guo, F. Bttcher, J. Hertkorn, J. N. Schmidt, M. Wenzel, H. P. Bchler, T. Langen, and T. Pfau, “The low-energy Goldstone mode in a trapped dipolar supersolid,” *Nature* **574**, 386 (2019).
 - [13] G. G. Batrouni and R. T. Scalettar, “Phase Separation in Supersolids,” *Phys. Rev. Lett.* **84**, 1599 (2000).
 - [14] F. Hbert, G. G. Batrouni, R. T. Scalettar, G. Schmid, M. Troyer, and A. Dorneich, “Quantum phase transitions in the two-dimensional hardcore boson model,” *Phys. Rev. B* **65**, 014513 (2001).
 - [15] K. K. Ng and Y. C. Chen, “Supersolid phases in the bosonic extended Hubbard model,” *Phys. Rev. B* **77**, 052506 (2008).
 - [16] L. Dang, M. Boninsegni, and L. Pollet, “Vacancy supersolid of hard-core bosons on the square lattice,” *Phys. Rev. B* **78**, 132512 (2008).
 - [17] S. J. Dong, W. Liu, X. F. Zhou, G. C. Guo, Z. W. Zhou, Y. J. Han, and L. He, “Peculiar supersolid phases induced by frustrated tunneling in the extended Bose-Hubbard model,” *Phys. Rev. B* **96**, 045119 (2017).
 - [18] Y. C. Chen and M. F. Yang, “Two supersolid phases in hard-core extended Bose-Hubbard model,” *J. Phys. Commun.* **1**, 035009 (2017).
 - [19] Y. C. Chen, R. G. Melko, S. Wessel, and Y. J. Kao, “Supersolidity from defect condensation in the extended boson Hubbard model,” *Phys. Rev. B* **77**, 014524 (2008).
 - [20] W. L. Tu, H. K. Wu, and T. Suzuki, “Frustration-induced supersolid phases of extended bose-hubbard model in the hard-core limit,” *arXiv: 1912.12464* (2019).
 - [21] T. Lahaye, C. Menotti, L. Santos, M. Lewenstein, and T. Pfau, “The physics of dipolar bosonic quantum gases,” *Rep. Prog. Phys.* **72**, 126401 (2009).
 - [22] B. Capogrosso-Sansone, C. Trefzger, M. Lewenstein, P. Zoller, and G. Pupillo, “Quantum phases of cold polar molecules in 2d optical lattices,” *Phys. Rev. Lett.* **104**, 125301 (2010).
 - [23] T. Ohgoe, T. Suzuki, and N. Kawashima, “Novel mechanism of supersolid of ultracold polar molecules in optical lattices,” *J. Phys. Soc. Jpn.* **80**, 113001 (2011).
 - [24] D. Yamamoto, G. Marmorini, and I. Danshita, “Quantum phase diagram of the triangular-lattice XXZ model in a magnetic field,” *Phys. Rev. Lett.* **112**, 127203 (2014).
 - [25] A. Macia, D. Hufnagl, F. Mazzanti, J. Boronat, and R. E. Zillich, “Excitations and Stripe Phase Formation in a Two-Dimensional Dipolar Bose Gas with Tilted Polarization,” *Phys. Rev. Lett.* **109**, 235307 (2012).
 - [26] T. Ohgoe, T. Suzuki, and N. Kawashima, “Quantum phases of hard-core bosons on two-dimensional lattices with anisotropic dipole-dipole interaction,” *Phys. Rev. A* **86**, 063635 (2012).
 - [27] A. Macia, J. Boronat, and F. Mazzanti, “Phase diagram of dipolar bosons in two dimensions with tilted polarization,” *Phys. Rev. A* **90**, 061601(R) (2014).
 - [28] C. Zhang, A. Safavi-Naini, A. M. Rey, and Capogrosso-Sansone B., “Equilibrium phases of tilted dipolar lattice bosons,” *New J. Phys.* **17**, 123014 (2015).
 - [29] D. Yamamoto, A. Masaki, and I. Danshita, “Quantum phases of hardcore bosons with long-range interactions on a square lattice,” *Phys. Rev. B* **86**, 054516 (2012).
 - [30] K. Misumi, T. Kaneko, and Y. Ohta, “Phase diagram of the frustrated square-lattice hubbard model: Variational cluster approach,” *J. Phys. Soc. Jpn.* **85**, 064711 (2016).
 - [31] X. Huo, Y. Y. Cui, D. Wang, and J. P. Lv, “Interacting hard-core bosons with anisotropic hopping: Checkerboard supersolid, order by disorder, and first-order phase transitions,” *Phys. Rev. B* **95**, 023613 (2017).
 - [32] Y. H. Chan, Y. J. Han, and L. M. Duan, “Supersolid and charge-density-wave states from anisotropic interaction in an optical lattice,” *Phys. Rev. A* **82**, 053607 (2010).
 - [33] M. P. Gelfand, R. R. P. Singh, and D. A. Huse, “Zero-temperature ordering in two-dimensional frustrated quantum heisenberg antiferromagnets,” *Phys. Rev. B* **40**, 10801 (1989).
 - [34] S. R. Hassan, L. de Medici, and A. M. S. Tremblay, “Supersolidity, entropy, and frustration: t-t'-v model of hard-core bosons on the triangular lattice,” *Phys. Rev. B* **76**, 144420 (2007).
 - [35] D. Yamamoto, I. Danshita, and C. A. R. S de Melo, “Dipolar bosons in triangular optical lattices: Quantum phase transitions and anomalous hysteresis,” *Phys. Rev. A* **85**, 021601(R) (2012).
 - [36] T. McIntosh, P. Pisarski, R. J. Gooding, and E. Zaremba, “Multisite mean-field theory for cold bosonic atoms in optical lattices,” *Phys. Rev. A* **86**, 013623 (2012).
 - [37] D. S. Lhmann, “Cluster gutzwiller method for bosonic lattice systems,” *Phys. Rev. A* **87**, 043619 (2013).
 - [38] M. Singh, T. Mishra, R. V. Pai, and B. P. Das, “Quantum phases of attractive bosons on a bose-hubbard ladder with three-body constraint,” *Phys. Rev. A* **90**, 013625 (2014).
 - [39] M. Moreno-Cardoner, H. Perrin, S. Paganelli, De Chiara G., and A. Sanpera, “Case study of the uniaxial anisotropic spin-1 bilinear-biquadratic heisenberg model on a triangular lattice,” *Phys. Rev. B* **90**, 144409 (2014).
 - [40] O. Jrgensen, K. Sengstock, and D. S. Lhmann, “Twisted complex superfluids in optical lattices,” *Sci. Rep.* **5**,

- 12912 (2015).
- [41] J. Jordan, R. Ors, G. Vidal, F. Verstraete, and J. I. Cirac, “Classical Simulation of Infinite-Size Quantum Lattice Systems in Two Spatial Dimensions,” *Phys. Rev. Lett.* **101**, 250602 (2008).
 - [42] R. Ors, “Tensor networks for complex quantum systems,” *Nat. Rev. Phys.* **1**, 538 (2019).
 - [43] P. Corboz, T. M. Rice, and M. Troyer, “Competing States in the $t - J$ Model: Uniform d -Wave State versus Stripe State,” *Phys. Rev. Lett.* **113**, 046402 (2014).
 - [44] T. Nishino and K. Okunishi, “Corner Transfer Matrix Renormalization Group Method,” *J. Phys. Soc. Jpn* **65**, 891 (1996).
 - [45] R. Ors and G. Vidal, “Simulation of two-dimensional quantum systems on an infinite lattice revisited: Corner transfer matrix for tensor contraction,” *Phys. Rev. B* **80**, 094403 (2009).
 - [46] H. C. Jiang, Z. Y. Weng, and T. Xiang, “Accurate Determination of Tensor Network State of Quantum Lattice Models in Two Dimensions,” *Phys. Rev. Lett.* **101**, 090603 (2008).
 - [47] H. J. Liao, J. G. Liu, L. Wang, and T. Xiang, “Differentiable Programming Tensor Networks,” *Phys. Rev. X* **9**, 031041 (2019).
 - [48] J. Hasik and G. B. Mbeng, <https://github.com/jurajHasik/peps-torch> (2020).
 - [49] T. Matsubara and H. Matsuda, “A Lattice Model of Liquid Helium, I,” *Prog. Theor. Phys.* **16**, 569 (1956).
 - [50] E. Lieb, T. Schultz, and D. Mattis, “Two soluble models of an antiferromagnetic chain,” *Ann. Phys.* **16**, 407 (1961).
 - [51] X. F. Zhang, R. Dillenschneider, Y. Yu, and S. Eggert, “Supersolid phase transitions for hard-core bosons on a triangular lattice,” *Phys. Rev. B* **84**, 174515 (2011).
 - [52] G. Masella, A. Angelone, F. Mezzacapo, G. Pupillo, and N. V. Prokofev, “Supersolid stripe crystal from finite-range interactions on a lattice,” *Phys. Rev. Lett.* **123**, 045301 (2019).